Nuclear Mathematical and Computational Sciences: A Century in Review, A Century Anew
Gatlinburg, Tennessee, April 6-11, 2003, on CD-ROM, American Nuclear Society, LaGrange Park, IL (2003)

A HYBRID NODAL METHOD FOR TIME-DEPENDENT INCOMPRESSIBLE FLOW IN TWO-DIMENSIONAL ARBITRARY GEOMETRIES

Allen J. Toreja
Lawrence Livermore National Laboratory
P.O. Box 808, L-038
Livermore, California 94551 U.S.A.
atoreja@llnl.gov

Rizwan-uddin *
Department of Nuclear, Plasma, and Radiological Engineering
University of Illinois at Urbana-Champaign
214 Nuclear Engineering Laboratory MC 234
103 South Goodwin Avenue
Urbana, Illinois 61801 U.S.A.
rizwan@uiuc.edu

ABSTRACT

A hybrid nodal-integral/finite-analytic method (NI-FAM) is developed for time-dependent, incompressible flow in two-dimensional arbitrary geometries. In this hybrid approach, the computational domain is divided into parallelepiped and wedge-shaped *space-time* nodes (cells). The conventional nodal integral method (NIM) is applied to the interfaces between adjacent parallelepiped nodes (cells), while a finite analytic approach is applied to the interfaces between parallelepiped and wedge-shaped nodes (cells). In this paper, the hybrid method is formally developed and an application of the NI-FAM to fluid flow in an enclosed cavity is presented. Results are compared with those obtained using a commercial computational fluid dynamics code.

Key Words: nodal method, arbitrary geometries, Navier-Stokes equations, incompressible flow

1. INTRODUCTION

Nodal methods have been developed for a wide range of problems of interest to nuclear scientists and engineers, including the Navier-Stokes equations, the convection-diffusion equation, and the multi-group neutron diffusion equations [2] [6] [9] [17]. The superior discretization scheme of the nodal methods provides an advantage over many conventional numerical methods in that nodal methods, by using coarse meshes, typically require less CPU time to achieve a given accuracy. However, nodal methods that depend upon a transverse integration step to reduce the governing partial differential equation(s) into ordinary differential equations, such as the nodal integral method, are limited to domains formed by the union of rectangular nodes (cells). Although nodal methods have been developed for specific non-rectangular geometries — such as cylindrical or hexagonal — only those based on the boundary fitted coordinate technique are applicable to domains of arbitrary geometry [8]. Hence, a numerical scheme that can relax the restriction on the geometry of the domain without sacrificing the nodal efficiency is desirable.

*Also, Computational Science and Engineering Program

Toreja and Rizwan-uddin [16] have recently proposed a hybrid nodal-integral/finite-analytic method (NI-FAM), which was successfully applied to steady-state and time-dependent convection-diffusion problems in arbitrary geometries. In this method, the conventional nodal integral method (NIM) [2] [9] is coupled to a finite analytic approach. Developed by Roscoe [11] and further extended by Chen [4] and others, the finite analytic approach introduces certain approximations so as to reduce the partial differential equation(s) into sub-problems (ordinary differential equations) that can be solved analytically. This particular step of the finite analytic approach achieves the same objective as the transverse-integration procedure of the nodal integral approach, and is not limited to regular geometries. The analytical solutions of these sub-problems are then used to formulate the algebraic representations of the governing partial differential equation(s) [4].

In the hybrid NI-FAM of Toreja and Rizwan-uddin [16], the computational domain is first divided into rectangular and triangular nodes (cells). The triangular nodes (cells) are restricted to the domain boundaries that are not parallel to the x or y axes. The conventional NIM is then applied to the interfaces between rectangular nodes (cells) while the finite analytic approach is applied to the triangular-rectangular node (cell) interfaces. Since the discrete variables in the NIM are the *transverse-integrated* (or *surface-averaged* or *edge-averaged*) quantities along the edges of the rectangular nodes (cells), the finite analytic approach must be developed in terms of transverse-integrated quantities, as well. This allows for the imposition of continuity conditions on the interfaces between triangular and rectangular nodes (cells).

Motivated by the success of the NI-FAM applications to the convection-diffusion equation, the hybrid NI-FAM is developed here to solve the time-dependent, incompressible Navier-Stokes equations in two-dimensional arbitrary geometries. This particular development of the NI-FAM will extend the efficiency of existing nodal methods for fluid flow applications [2] [17] [20] to complex geometries without sacrificing the nodal efficiency. Furthermore, the potential combination of the NI-FAM for the Navier-Stokes equations with the NI-FAM for the convection-diffusion equation will allow the nodal method to accurately and efficiently simulate a wide range of coupled fluid flow and heat transfer problems. Applications of this type will be particularly useful in coupled neutronic/thermal-hydraulic nodal analyses for the next generation of nuclear reactors.

2. FORMALISM

2.1. The Time-Dependent Incompressible Navier-Stokes Equations

The two-dimensional, time-dependent, incompressible Navier-Stokes momentum and Poisson pressure equations are

$$\frac{\partial u}{\partial t} + u\frac{\partial u}{\partial x} + v\frac{\partial u}{\partial y} = \nu\left(\frac{\partial^2 u}{\partial x^2} + \frac{\partial^2 u}{\partial y^2}\right) - \frac{1}{\rho}\frac{\partial \rho}{\partial x} + g_x \tag{1}$$

$$\frac{\partial v}{\partial t} + u\frac{\partial v}{\partial x} + v\frac{\partial v}{\partial y} = \nu\left(\frac{\partial^2 v}{\partial x^2} + \frac{\partial^2 v}{\partial y^2}\right) - \frac{1}{\rho}\frac{\partial \rho}{\partial y} + g_y \tag{2}$$

$$-\frac{1}{\rho}\left(\frac{\partial^2 p}{\partial x^2} + \frac{\partial^2 p}{\partial y^2}\right) = \left(\frac{\partial u}{\partial x}\right)^2 + \left(\frac{\partial v}{\partial y}\right)^2 + 2\left(\frac{\partial u}{\partial y}\frac{\partial v}{\partial x}\right) - \frac{\partial g_x}{\partial x} - \frac{\partial g_y}{\partial y} \tag{3}$$

where ν is the viscosity, ρ is the density, u and v are the velocities in the x and y directions, respectively, and, g_x and g_y are the body forces in the x and y directions respectively. The Poisson pressure equation is derived through the combination of the two momentum equations and the application of the continuity

equation [4] [12]. The Poisson pressure equation provides an explicit equation for the pressure, and for the purposes of this paper, Eqs. (1)-(3) will be referred to as the "Navier-Stokes equations".

Before starting the development of the hybrid NI-FAM for the incompressible Navier-Stokes equations, the momentum equations are rewritten in a modified form by subtracting from both sides of the equations linear convection terms based on the constant velocities, u^p and v^p,

$$\frac{\partial u}{\partial t} + u\frac{\partial u}{\partial x} + v\frac{\partial u}{\partial y} - u^p\frac{\partial u}{\partial x} - v^p\frac{\partial u}{\partial y} = \nu\left(\frac{\partial^2 u}{\partial x^2} + \frac{\partial^2 u}{\partial y^2}\right) - \frac{1}{\rho}\frac{\partial \rho}{\partial x} + g_x - u^p\frac{\partial u}{\partial x} - v^p\frac{\partial u}{\partial y} \tag{4}$$

$$\frac{\partial v}{\partial t} + u\frac{\partial v}{\partial x} + v\frac{\partial v}{\partial y} - u^p\frac{\partial v}{\partial x} - v^p\frac{\partial v}{\partial y} = \nu\left(\frac{\partial^2 v}{\partial x^2} + \frac{\partial^2 v}{\partial y^2}\right) - \frac{1}{\rho}\frac{\partial \rho}{\partial y} + g_y - u^p\frac{\partial v}{\partial x} - v^p\frac{\partial v}{\partial y}. \tag{5}$$

As in the schemes based on delayed coefficients [18], when discretizing Eqs. (4)-(5), u^p and v^p will be defined as node-averaged constant velocities based on velocity values from the previous time step. Explicit expressions for these constants are given later.

Use of the Poisson pressure equation and the introduction of the convection terms based on the node-averaged velocities from the previous time step lead to a nodal scheme in terms of primitive variables (u, v, p) as well as node interior solutions that are symmetric in the x and y directions. Furthermore, instead of linear or quadratic solutions [2] [20], these solutions are of a *linear + exponential* form. This formulation of the nodal integral method for the incompressible Navier-Stokes equations for regular geometries is developed in [17].

2.2. The Hybrid NI-FAM for the Time-Dependent Incompressible Navier-Stokes Equations

First, the time axis is discretized with a constant time interval of 2τ. The discretization of the space-time domain with an arbitrarily-shaped, two-dimensional, spatial domain then proceeds by dividing the region into *parallelepiped* and *wedge-shaped* space-time nodes. The wedge-shaped nodes are restricted to the spatial boundaries that are not parallel to the x or y axes. For the parallelepiped nodes, a local coordinate system is defined with the origin at the center of the node. For the wedge-shaped nodes, a local coordinate system is defined with the origin at the center of the diagonal edge. Schematic diagrams of one type of wedge-shaped space-time node and a parallelepiped space-time node along with their local coordinate system and associated discrete variables are shown in Figs. 1-2. The definitions of the discrete variables are given later.

In the NI-FAM, the set of equations for the unknown discrete variables associated with the interface between two adjacent parallelepiped nodes are derived using the nodal integral method (NIM) of Wang [17]. For the interface between a wedge-shaped node and a parallelepiped node, a new type of finite analytic method, motivated by the hybrid method for the convection-diffusion equation [13], is developed here. As in the NIM, the procedure in the new hybrid method for the wedge-shaped-parallelepiped-node interface consists of three major steps. In step one, the governing partial differential equations are reduced to a set of ordinary differential equations. The second step is to analytically solve these ordinary differential equations and eliminate intermediate unknowns. In the third step, the algebraic difference relations for the discrete variables on the interface between the two different types of nodes are obtained by imposing continuity of the flux, i.e., by equating the derivatives from both sides of the interface.

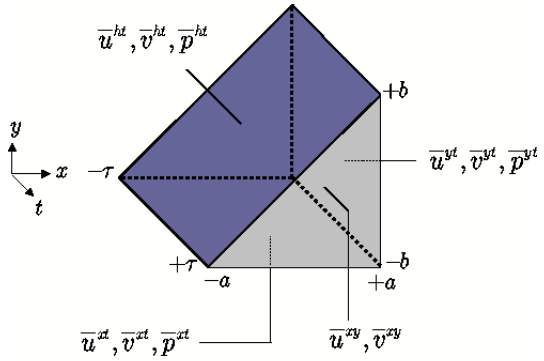

Figure 1. Wedge-shaped space-time node

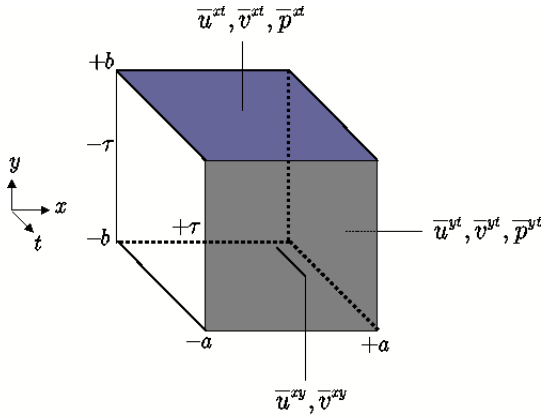

Figure 2. Parallelepiped space-time node

Step 1

The formal derivation begins by approximating the velocities and pressure over the wedge-shaped node as a sum of unknown (single-variable) functions and a constant,

$$u(x,y,t) \cong u_x(x) + u_y(y) + u_t(t) + u_0 \tag{6}$$

$$v(x,y,t) \cong v_x(x) + v_y(y) + v_t(t) + v_0 \tag{7}$$

$$p(x,y) \cong p_x(x) + p_y(y) + p_0. \tag{8}$$

The approximations in Eqs. (6)-(8) are similar to those made in the finite analytic method of Chen [4]. Anticipating that the finite analytic approach for the wedge-shaped node will be coupled with the NIM for the parallelepiped node, the functions, $u_x(x)$, $u_y(y)$, $u_t(t)$, are approximations to single variable transverse-averaged velocities in the wedge-shaped node. These functions respectively correspond to the transverse-integrated functions, $\bar{u}^{yt}(x)$, $\bar{u}^{xt}(y)$, $\bar{u}^{xy}(t)$, of a parallelpiped node. The functions for the v velocity and pressure in Eqs. (7)-(8) are similarly defined. As will be shown, the finite analytic approach of the wedge-shaped node is developed in terms of these approximate transverse-integrated variables so that the finite analytic approach of the wedge-shaped node can be coupled with the nodal approach of the adjacent parallelepiped node.

The finite analytic approximations are first substituted into the u momentum equation, Eq. (4), which leads to the following ordinary differential equation,

$$\nu\left(\frac{d^2u_x}{dx^2} + \frac{d^2u_y}{dy^2}\right) - u^p\frac{du_x}{dx} - v^p\frac{du_y}{dy} = \frac{du_t}{dt} + K^u(x,y,t) \tag{9a}$$

where

$$K^u(x,y,t) = u\frac{du_x}{dx} + v\frac{du_y}{dy} - u^p\frac{du_x}{dx} - v^p\frac{du_y}{dy} + \frac{1}{\rho}\frac{dp_x}{dx} - g_x. \tag{9b}$$

The term, K^u, in Eq. (9a) resembles a "source/sink-like" term. Motivated by a similar step performed in the NI-FAM for the convection-diffusion equation [15], the following approximation is introduced,

$$K^u(x,y,t) \cong R^u(x) + S^u(y) - T^u(t), \tag{10}$$

where $R^u(x)$, $S^u(y)$, and $T^u(t)$, are unknown functions that are referred to as the "sub-source terms" for the u momentum equation. (As a matter of convenience, the sub-source term, $T^u(t)$, is subtracted, rather than added, for it makes the right hand side of Eq. (14a) positive rather than negative.) Substitution of Eq. (10) into Eq. (9a) leads to the following equation,

$$\frac{du_t(t)}{dt} + R^u(x) + S^u(y) - T^u(t) = \nu\left(\frac{d^2u_x(x)}{dx^2} + \frac{d^2u_y(y)}{dy^2}\right) - u^p\frac{du_x}{dx} - v^p\frac{du_y}{dy}. \tag{11}$$

Equation (11) is then split into three ordinary differential equations. Using the boundary/initial condititions associated with the wedge-shaped node of Fig. 1, the three ordinary differential equations and associated boundary/initial conditions are

$$\nu\frac{d^2u_x}{dx^2} - u^p\frac{du_x}{dx} = R^u(x) \tag{12a}$$

$$u_x(x=0) = \overline{u}^{ht} \tag{12b}$$

$$u_x(x=a) = \overline{u}^{yt} \tag{12c}$$

$$\nu\frac{d^2u_y}{dy^2} - v^p\frac{du_y}{dy} = S^u(y) \tag{13a}$$

$$u_y(y=-b) = \overline{u}^{xt} \tag{13b}$$

$$u_y(y=0) = \overline{u}^{ht} \tag{13c}$$

and

$$\frac{du_t}{dt} = T^u(t) \tag{14a}$$

$$u_t(t=-\tau) = \overline{u}^{xy}. \tag{14b}$$

This same procedure is applied to Eq. (5), resulting in the corresponding ordinary differential equations for the v velocity, which have forms similar to Eqs. (12a)-(14b). The same procedure is again applied to the Poisson pressure equation, which yields the following ordinary differential equations,

$$-\frac{1}{\rho}\frac{d^2p_x}{dx^2} = G(x) \tag{15a}$$

$$p_x(x=0) = \overline{p}^{ht} \tag{15b}$$

$$p_x(x=a) = \overline{p}^{yt} \tag{15c}$$

$$-\frac{1}{\rho}\frac{d^2p_y}{dy^2} = H(y) \tag{16a}$$

$$p_y(y=-b) = \overline{p}^{xt} \tag{16b}$$

$$p_y(y=0) = \overline{p}^{ht} \tag{16c}$$

where the functions, $G(x)$ and $H(y)$ are the sub-source terms for the Poisson pressure equation.

For the wedge-shaped node of Fig. 1, the formal definitions of the discrete variables associated with the transverse-integrated u velocity are

$$\overline{u}^{xt} \equiv \frac{1}{4a\tau}\int_{-a}^{a}\int_{-\tau}^{\tau} u(x, y=-b, t)\, dt\, dx, \tag{17}$$

$$\overline{u}^{yt} \equiv \frac{1}{4b\tau}\int_{-b}^{b}\int_{-\tau}^{\tau} u\left(x=a,y,t\right)\,dt\,dy, \tag{18}$$

$$\overline{u}^{ht} \equiv \frac{1}{4a\tau}\int_{-a}^{a}\int_{-\tau}^{\tau} u\left(x,y=\frac{b}{a}x,t\right)\,dt\,dx, \tag{19}$$

and

$$\overline{u}^{xy} \equiv \frac{1}{2ab}\int_{-a}^{a}\int_{-b}^{\frac{b}{a}x} u\left(x,y,t=+\tau\right)\,dy\,dx. \tag{20}$$

The discrete variables associated with the transverse-integrated v velocity and pressure are similarly defined. The single variable functions in the finite analytic approximations correspond to the transverse-integrated functions of the NIM, allowing the use of the surface-averaged velocities and pressures in the boundary conditions of the above differential equations. Using the transverse-integrated variables in the boundary conditions thus facilitates the coupling of the finite analytic approach of the wedge-shaped node with the nodal approach of the adjacent parallelepiped node. In addition, the boundary conditions at $x = 0$ and $y = 0$ use a new set of transverse-integrated variables, namely, $\overline{u}^{ht}$, $\overline{v}^{ht}$, $\overline{p}^{ht}$. These transverse-integrated variables represent the velocities and pressure averaged over the diagonal edge of the wedge-shaped node.

Step 2

As outlined, the second major step of the NI-FAM for the Navier-Stokes equations is to analytically solve the ordinary differential equations. In each of the ordinary differential equations, the right hand side consists of an unknown inhomogeneous term. Using a similar procedure from the NIM, these unknown inhomogeneous terms are expanded in Legendre polynomials and trucated at the zeroth order. Hence, the sub-source terms from Eq. (12a), Eq. (13a), Eq. (14a), Eq. (15a), and Eq. (16a) — $R^u(x)$, $S^u(y)$, $T^u(t)$, $G(x)$, $H(y)$ — are replaced with the sub-source constants, R_0^u, S_0^u, T_0^u, G_0, and H_0, respectively. These sub-source constants are not explicitly specified, and are eliminated later.

The second-order differential equations for the transverse-integrated velocities (Eq. (12a), Eq. (13a), and the corresponding v velocity equations) lead to solutions of *linear+exponential* form,

$$f_n\left(\eta\right) = C_0 - \frac{g_o^f}{f^p}\eta + C_1\exp\left(\frac{f^p}{\nu}\eta\right) \tag{21}$$

where f is either u or v, g is either R or S, η is either x or y, and C_0 and C_1 are constants of integration. The first-order velocity differential equations (Eq. (14a), and the corresponding v velocity equation) lead to a simple linear solution of the following form,

$$f_t\left(t\right) = D_0 + T_0^f t \tag{22}$$

where D_0 is the constant of integration and the definitions of the previous case apply here as well. The two remaining second order differential equations for the pressure (Eq. (15a), Eq. (16a)) lead to second-order polynomial solutions for the following form,

$$p_\eta\left(\eta\right) = E_0 + E_1\eta - \frac{\rho h_0}{2}\eta^2 \tag{23}$$

where E_0 and E_1 are the constants of integration, h is G or H, and η is x or y.

The constants of integration are eliminated by imposing the initial and boundary conditions. Hence, the local node interior solutions are written in terms of transverse-integrated variables along the node edges

(the discrete unknowns) as well as the unknown sub-source terms. Assuming that the transverse-integrated variables along the diagonal edge of the wedge-shaped node are known (Dirichlet boundary conditions), the (eight) analytical solutions corresponding to the forms in Eqs. (21)-(23) contain eight unknown transverse-integrated variables ($\overline{u}^{xt}$, $\overline{u}^{yt}$, $\overline{u}^{xy}$, $\overline{v}^{xt}$, $\overline{v}^{yt}$, $\overline{v}^{xy}$, $\overline{p}^{xt}$, $\overline{p}^{yt}$) and eight unknown sub-source constants (R_0^u, S_0^u, T_0^u, R_0^v, S_0^v, T_0^v, G_0, H_0). As part of the second step in the development of the NI-FAM, the unknown sub-source constants must be eliminated in favor of the unknown transverse-integrated discrete variables. Once the unknown sub-source constants have been eliminated, continuity conditions will be imposed (in the final step) between the wedge-shaped node and the adjacent parallelepiped nodes thereby yielding the necessary algebraic difference relations.

To eliminate the unknown sub-source constants, two types of constraints are introduced. These constraints are, in principle, the same as those applied in the conventional NIM, namely satisfying each governing equation over the node in an integral sense and imposing the uniqueness of node-averaged quantities. The first type of constraint uses an averaging operator that is defined as

$$\overline{f}^{xyt} = \frac{1}{2ab\tau} \int_{-\tau}^{\tau} \int_{-b}^{0} \int_{0}^{a} f\left(x, y, t\right)\, dx\, dy\, dt. \tag{24}$$

This operator yields the average value of $f(x, y, t)$ over the wedge-shaped node. This operator is first applied to the u momentum equation, Eq. (9b). To carry out the integration, the sub-source terms in Eq. (10) are replaced with the appropriate sub-source constants, and the average of the convection terms of the form, $u\frac{du_x}{dx}$, is approximated by the product of the averages, which is known to be a second order approximation [9]. For Eq. (9b), the averaging operator yields the following

$$\left(u^o - u^p\right)\left(\frac{\overline{u}^{yt} - \overline{u}^{ht}}{a}\right) + \left(v^o - v^p\right)\left(\frac{\overline{u}^{ht} - \overline{u}^{xt}}{b}\right) + T_o^u = R_o^u + S_o^u - \frac{1}{\rho}\left(\frac{\overline{p}^{yt} - \overline{p}^{ht}}{a}\right) + \overline{g}_x^{xyt}, \tag{25}$$

where u^o and v^o are the node-averaged u and v velocities from the current time step, respectively. These particular node-averaged velocities result from the approximation of the convection terms in the averaging operator. The averaging operator is then applied to the the v momentum and pressure equations which yield the corresponding v momentum and pressure analogs of Eq. (25). The expressions obtained from the averaging operator can be interpreted as the Navier-Stokes equations averaged over the wedge-shaped space-time node.

The second type of constraint used to eliminate the sub-source constants requires that for each wedge-shaped node there should be a unique node-averaged u velocity, v velocity, and pressure. Therefore, for the u velocity, the uniqueness constraints are

$$\frac{1}{a}\int_{0}^{a} u_x\left(x\right)\, dx = \frac{1}{\tau}\int_{-\tau}^{\tau} u_t\left(t\right)\, dt, \tag{26a}$$

$$\frac{1}{b}\int_{-b}^{0} u_y\left(y\right)\, dy = \frac{1}{\tau}\int_{-\tau}^{\tau} u_t\left(t\right)\, dt. \tag{26b}$$

Similar uniqueness constraints are defined for the v velocity and the pressure.

Using these eight constraint equations, the unknown sub-source terms are eliminated. Thus, the local interior node solutions can then be expressed solely in terms of the initial and boundary conditions along the node edges.

Step 3

In the third and final step of the development, the algebraic difference equations for the transverse-integrated variables on the interface between the two types of nodes are developed. In Fig. 3, the projections of a wedge-shaped node and the adjacent parallelepiped nodes onto the xy plane are shown. For the wedge-shaped node, (i, j), and the adjacent parallelepiped node on the right, $(i+1, j)$, the transverse-integrated variables on the interface between the two nodes are $\overline{u}^{yt}_{i,j}$, $\overline{v}^{yt}_{i,j}$, and $\overline{p}^{yt}_{i,j}$, where the subscripts are the spatial indices. The algebraic difference equation for the variable, $\overline{u}^{yt}_{i,j}$, is derived by imposing the C^1 continuity condition, i.e., by taking the derivative of the solution in the wedge-shaped node, $u_{x,i,j}(x)$, evaluating it at the right edge, $x = a_{i,j}$, and equating it to the derviative of the corresponding solution in the parallelepiped node on the right of the wedge-shaped node, $\overline{u}^{yt}_{i+1,j}$, evaluated on the left edge, $x = -a_{i+1,j}$. That is,

$$\left.\frac{du_{x,i,j}(x)}{dx}\right|_{x=a_{i,j}} = \left.\frac{d\overline{u}^{yt}_{i+1,j}(x)}{dx}\right|_{x=-a_{i+1,j}}, \tag{27}$$

where the transverse-integrated function, $\overline{u}^{yt}_{i+1,j}(x)$, is obtained through the application of the NIM to the parallepiped node [17]. Solving Eq. (27) for the transverse-integrated variable, $\overline{u}^{yt}_{i,j}$, yields an algebraic difference equation of the following form,

$$\begin{aligned}\overline{u}^{yt}_{i,j} &= \left(A^{(1)}_{i,j}\right)\overline{u}^{ht}_{i,j} + \left(A^{(2)}_{i,j}\right)\overline{u}^{yt}_{i+1,j} + \left(A^{(3)}_{i,j}\right)\overline{u}^{xy}_{i,j,k} \\ &\quad + \left(A^{(4)}_{i,j}\right)\overline{u}^{xy}_{i+1,j,k} + \left(A^{(5)}_{i,j}\right)\overline{u}^{xy}_{i,j,k-1} + \left(A^{(6)}_{i,j}\right)\overline{u}^{xy}_{i+1,j,k-1}\end{aligned} \tag{28}$$

where the coefficients, $A^{(m)}_{i,j}(m = 1, 2, 3, \ldots 6)$, are constants that depend on the node dimensions, viscosity and the nodal velocities from the previous timp step, u^p and v^p. The expressions for the coefficients, $A^{(m)}_{i,j}$, are given in [15]. The third subscript, k, which appears in the transverse-integrated variable, $\overline{u}^{xy}_{i,j,k}$ refers to the current time step. Repeating this procedure for the transverse-integrated variables, $\overline{v}^{yt}_{i,j}$ and $\overline{p}^{yt}_{i,j}$, yields the corresponding algebraic difference equations for these variables. Furthermore, repeating this procedure in the vertical direction for the wedge-shaped node, (i, j), and the adjacent parallelepiped node on the bottom, $(i, j-1)$, yields the algebraic equations for the transverse-integrated variables, $\overline{u}^{xt}_{i,j-1}$, $\overline{v}^{xt}_{i,j-1}$, and $\overline{p}^{xt}_{i,j-1}$.

Since the differential equations for $u_t(t)$ and $v_t(t)$ are first order, the algebraic difference equations for the transverse-integrated variables, $\overline{u}^{xy}_{i,j,k}$ and $\overline{v}^{xy}_{i,j,k}$, are obtained by simply evaluating the wedge-shaped node solutions, $u_{t,i,j}(t)$ and $v_{t,i,j}(t)$, at $t = +\tau$. Defining $u_{t,i,j}(t = +\tau) \equiv \overline{u}^{xy}_{i,j,k}$ and $u_{t,i,j}(t = -\tau) \equiv \overline{u}^{xy}_{i,j,k-1}$, the difference equation for the transverse-integrated variable, $\overline{u}^{xy}_{i,j,k}$, is found to be of the following form,

$$\begin{aligned}\overline{u}^{xy}_{i,j,k} &= \left(B^{(1)}_{i,j}\right)\overline{u}^{xy}_{i,j,k-1} + \left(B^{(2)}_{i,j}\right)\overline{u}^{ht}_{i,j} + \left(B^{(3)}_{i,j}\right)\overline{u}^{yt}_{i,j} \\ &\quad + \left(B^{(4)}_{i,j}\right)\overline{u}^{xt}_{i-1,j} + \left(B^{(5)}_{i,j}\right)\overline{p}^{ht}_{i,j} + \left(B^{(6)}_{i,j}\right)\overline{p}^{yt}_{i,j} + \left(B^{(7)}_{i,j}\right)\overline{g}^{xyt}_{x,i,j,k}\end{aligned} \tag{29}$$

where the coefficients, $B^{(m)}_{i,j}(m = 1, 2, 3 \ldots 7)$, are constants that depend on the node dimensions, viscosity and the nodal velocities, u^p, v^p, u^o, and v^o. The expressions for the coefficients, $B^{(m)}_{i,j}$, are also given in [15]. Since the coefficients, $B^{(m)}_{i,j}(m = 1, 2, 3 \ldots 7)$, are dependent on node-averaged velocities of the

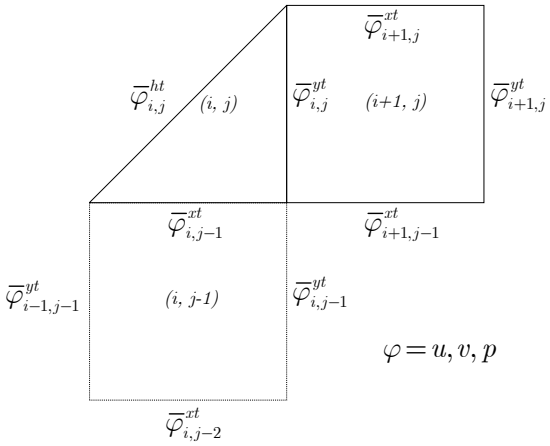

Figure 3. Projection of wedge-shaped space-time node, (i, j), and its adjacent parallelepiped nodes, $(i + 1, j)$ and $(i, j - 1)$, onto the xy plane.

current timestep, these coefficients must be evaluated every time the transverse-integrated discrete variables are updated. The equation for the transverse-integrated variable, $\overline{v}^{xy}_{i,j,k}$, has a form similar to Eq. (29).

The node-averaged velocities from the previous time step, u^p and v^p, are introduced in Eqs. (4) and (5). The node-averaged velocities at the current time step, u^o and v^o, are introduced in Eq. (25). These node-averaged velocities also appear in the application of the conventional NIM to the parallelepiped space-time node [15] [17]. In the conventional NIM, the node-averaged u velocity at the current (k) time step, u^o, for the parallelepiped node, (i, j, k) is defined as the perimeter-based average of the four edge-averaged velocities,

$$u^o_{i,j,k} = \frac{(2b_{i,j,k})\,\overline{u}^{yt}_{i,j,k} + (2b_{i-1,j,k})\,\overline{u}^{yt}_{i-1,j,k} + (2a_{i,j,k})\,\overline{u}^{xt}_{i,j,k} + (2a_{i,j-1,k})\,\overline{u}^{yt}_{i,j-1,k}}{2b_{i,j,k} + 2b_{i-1,j,k} + 2a_{i,j,k} + 2a_{i,j-1,k}}. \tag{30}$$

The node-averaged velocity from the previous $(k - 1)$ time step, u^p, has the same form as Eq. (30) with the subscript, k, replaced by $k - 1$. Furthermore, the node-averaged velocities, v^o and v^p, are similarly defined. To maintain consistency with the NIM, a perimeter-based average is also used to define the node-averaged velocities for the wedge-shaped node. Thus, for the wedge-shaped node of Fig. 1, the node-averaged u velocity at the current time step, u^o is defined as

$$\begin{aligned} u^o_{i,j,k} \;=\; & \frac{1}{2a_{i,j,k} + 2b_{i,j,k} + \sqrt{(2a_{i,j,k})^2 + (2b_{i,j,k})^2}} \cdot \\ & \left[(2b_{i,j,k})\,\overline{u}^{yt}_{i,j,k} + (2a_{i,j,k})\,\overline{u}^{xt}_{i,j-1,k} + \left(\sqrt{(2a_{i,j,k})^2 + (2b_{i,j,k})^2} \right) \overline{u}^{ht}_{i,j,k} \right]. \end{aligned} \tag{31}$$

Likewise, the node-averaged u velocity of the wedge-shaped node from the previous $(k - 1)$ time step, u^p, has the same form as Eq. (31) with the subscript, k, replaced by $k - 1$. The node-averaged v velocities, v^o and v^p, are similarly defined, as well.

Although the velocity (or its derivative) is frequently known on the boundary, pressure on the boundary is typically not known and must be evaluated. Using an approach similar to the one used by Chen [4] in the *diagonal Cartesian method*, an equation for the transverse-integrated pressure on the diagonal surface, $\overline{p}^{ht}_{i,j}$,

is obtained using the continuity equation. The derivation of this scheme for pressure on the boundary can be found in [15].

The development above corresponds only to one type of wedge-shaped node. In practice, four types of wedge-shaped nodes are required to discretize any arbitrary geometry in two spatial dimensions. The remaining types of wedge-shaped nodes are described in [15]. The hybrid NI-FAM for these remaining wedge-shaped nodes are developed in the same manner as the derivation outlined here.

3. NUMERICAL RESULTS AND DISCUSSION

The test problem solved using the hybrid NI-FAM for the Navier-Stokes equations is that of flow inside an enclosed five-sided cavity, shown in Fig. 4. In this problem, the bottom of the cavity moves to the left with a constant velocity, while the remaining four sides are stationary. This problem is similar to the classical problem of flow inside an enclosed square cavity in which the top plate moves with a constant velocity to the right [3] [7] [10]. In both, this problem and the classical problem, the shear created by the moving plate leads to steady-state recirculating flow for low Reynolds numbers.

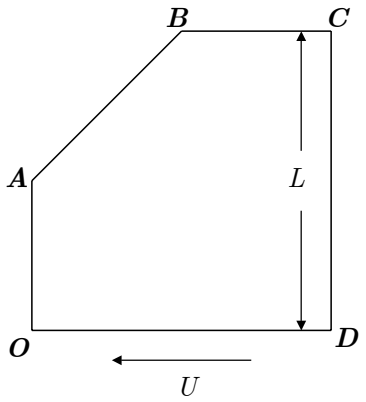

Figure 4. Schematic digaram of the five-sided cavity

In Fig. 4, the line segments, *OD* and *CD*, have a length of $L = 1$, while the segments, *OA* and *BC*, have a length of $L/2 = 0.5$. The segment *AB* forms a 45^o angle with the horizontal. No slip boundary conditions are imposed on all five walls. Hence, Dirichlet boundary conditions of $\vec{V} = 0$ are imposed along segments *OA, AB, BC*, and *CD*, while the velocity along segment *OD* is equal to the velocity of the bottom plate, U. Furthermore, the pressure values on all five walls are treated as unknowns.

Using a constant bottom plate velocity of $U = 1$, the flow field is simulated using the NI-FAM on three meshes of varying resolution. The details of the specific meshes are summarized in Table I. Mesh A is the coarsest mesh with 85 parallelepiped nodes and 5 wedge-shaped nodes, while mesh C has the highest resolution with 1390 parallelepiped nodes and 20 wedge-shaped nodes. The Reynolds number for these simulations is defined as $Re = \frac{UL}{\nu} = \frac{1}{\nu}$. A steady-state flow distribution is calculated on these meshes by assuming quiescent initial conditions $(u = v = p = 0)$ and marching in time until a non-transitory solution is reached. In this problem, the final time, t_f, at which a non-transitory flow field develops is dependent on the node size of the mesh and the time step used. The specific final time and time step used for each flow simulation is summarized in Table II.

A flow simulation on mesh A for a Reynolds number of $Re = 1$ was performed first, although these results

are not presented here. At such a low Reynolds number, it is expected that the velocity distribution in the enclosed cavity follow the outline of the cavity without producing any secondary vortices. These expectations are confirmed.

The results of the flow simulations for higher Reynolds numbers are shown in Figs. 5-8. Results are reported for flow simulated on meshes A and C at Reynolds numbers of $Re = 400$ and $Re = 1000$, respectively. For mesh B, results are reported for both Reynolds numbers. In these figures, two flow maps are presented for each simulation. In order to view the structure of the flow field clearly, velocity vectors of constant length are used in the top flow maps. The variation in the speed of the flow field is represented in the bottom flow maps where the velocity vector lengths are proportional to the magnitude of the velocity.

Table I. Mesh specifications for the five-sided cavity problem

Mesh	Δx	Number of wedge-shaped nodes	Total number of nodes
A	0.1	5	90
B	0.05	10	355
C	0.025	20	1410

Table II. Final times and time steps

Mesh	Re	Final Time	Δt
A	400	200	0.5
B	400	200	0.25
B	1000	250	0.0625
C	1000	100	0.03125

When the Reynolds number is $Re = 400$ and larger, the flow field becomes more complex producing a primary vortex that occupies a large region of the cavity and a secondary vortex that is situated near the top of the cavity, as shown in Figs. 5-8. This secondary vortex, has an oblong shape and is accompanied by a well-defined flow separation point on the right boundary. Although the secondary vortex is relatively large, the speed in this vortex is significantly smaller than the speed of the primary vortex, as indicated in Figs. 5-8 by the smaller arrows near the top of the cavity. Similar flow separation patterns have been reported by Darr [5] in trapezoidal cavities.

To analyze and compare the NI-FAM predictions, the center of the primary vortex and the location of the flow separation along the right boundary have been calculated. These points can be determined by using linear interpolation to calculate where the u and v velocities become zero. These calculations are summarized in Tables III- IV.

Figure 5 shows the flow maps for the velocity distribution calculated on mesh A. Figure 6 shows the corresponding flow maps for mesh B.[†] The flow structure predicted by the NI-FAM on mesh B in general agrees with the flow structure calculated on mesh A. However, as indicated in Table III, the simulation carried out on mesh B predicts the center of the primary vortex to be higher than that predicted by mesh A.

[†]The arrows in Fig. 5(b) that are of the same size as the arrows in Fig. 6(b) do not represent the same speed.

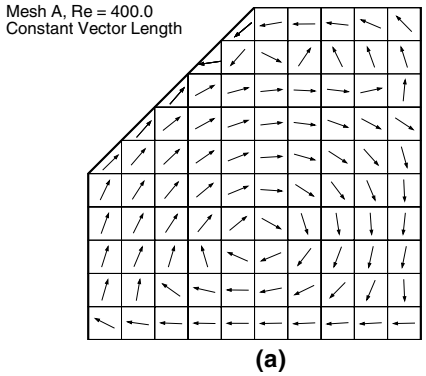

Figure 5. Flow maps for mesh A at $Re = 400$.

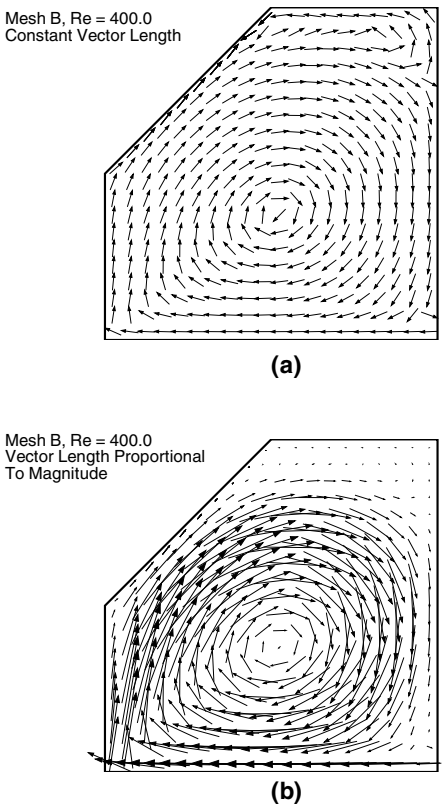

Figure 6. Flow maps for mesh B at $Re = 400$.

Morever, the results in Table IV show that the location of the flow separation on the right boundary of mesh B is closer to the top wall, which suggests that the secondary vortex as predicted on mesh B is slightly smaller. Figure 7 shows the flow maps for the velocity field as calculated on mesh B for a Reynolds number of $Re = 1000$. At this higher Reynolds number, the general structure of the flow field is similar to the flow field at a Reynolds number of $Re = 400$. However at $Re = 1000$, the separation point has moved further down the right boundary indicating that the size of the secondary vortex at $Re = 1000$ is significantly larger than the secondary vortex for $Re = 400$. In Fig. 8, the flow maps of the velocity field as predicted by the NI-FAM on mesh C for a Reynolds number of $Re = 1000$ are shown.[‡] The flow structure predicted by the NI-FAM on mesh B is very similar to the flow structures predicted on mesh C. The location of the primary vortex as well as the separation point predicted by the NI-FAM on mesh B are very close to those predicted on mesh C, which suggests that the resolution of mesh B is adequate.

Table III. Location of primary vortex center

Re	Mesh A	Mesh B	Mesh C
400	$(0.507, 0.307)$	$(0.513, 0.376)$	N/A
1000	N/A	$(0.493, 0.367)$	$(0.482, 0.369)$

To confirm the existence of the secondary vortex in the five-sided cavity and to independently verify the

[‡]The arrows in Fig. 7(b) that are of the same size as the arrows in Fig. 8(b) do not represent the same speed.

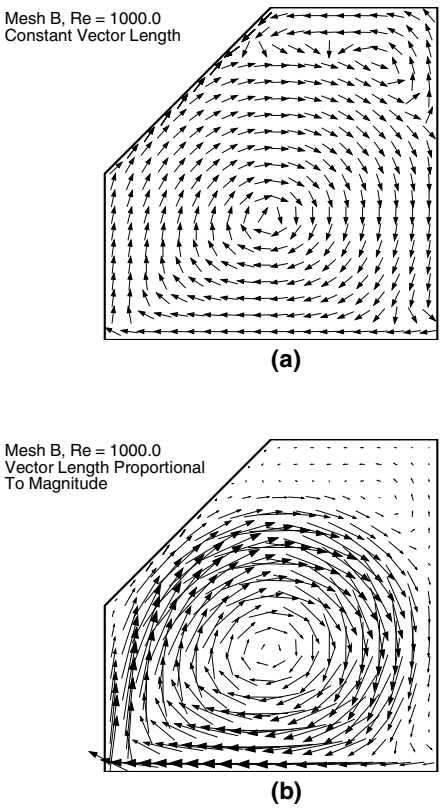

Figure 7. Flow maps for mesh B at $Re = 1000$.

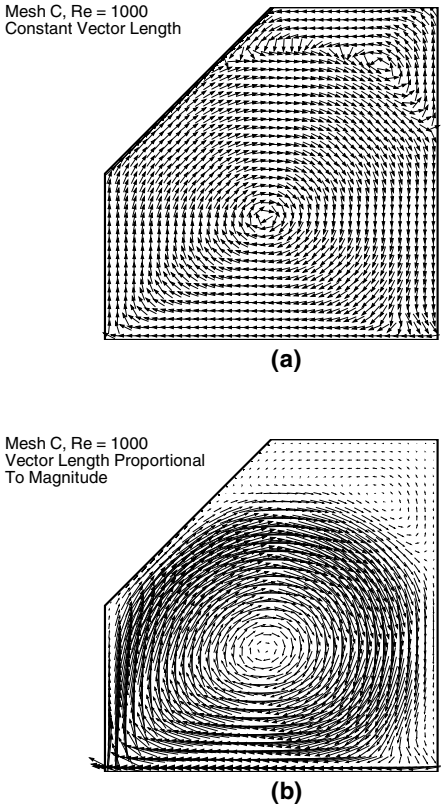

Figure 8. Flow maps for mesh C at $Re = 1000$.

Table IV. Location of flow separation

Re	Mesh A	Mesh B	Mesh C
400	$y = 0.682$	$y = 0.789$	N/A
1000	N/A	$y = 0.648$	$y = 0.634$

predictions of the NI-FAM, the steady-state flow in the enclosed cavity is calculated using the commercial computational fluid dynamics software package, *CFX* [1]. Unlike the NI-FAM simulations, the *CFX* simulations directly calculate the steady-state flow rather than march in time until a non-transitory flow is obtained. The results of the *CFX* calculations for Reynolds numbers, $Re = 400$ and $Re = 1000$ are presented in Figs. 9 and 10 respectively. (The "white strip" that runs from the top of the cavity to the bottom left corner in Figs. 9 and 10 is an artifact of the block generation and subsequent mesh generation algorithm in *CFX*.) The flow fields calculated by the NI-FAM and those predicted by *CFX* for these two Reynolds numbers agree quite well with each other. It should be noted that although the NI-FAM predictions on meshes B and C are consistent with the *CFX* results, the flow field calculated by the NI-FAM on mesh A is less accurate as indicated by the slightly lower location of the primary vortex. Clearly, the node size of the mesh A ($\Delta x = 0.1$) is too coarse for a Reynolds number of $Re = 400$. Although mesh A is too coarse to produce quantitatively accurate results, the flow field is nevertheless qualitatively correct.

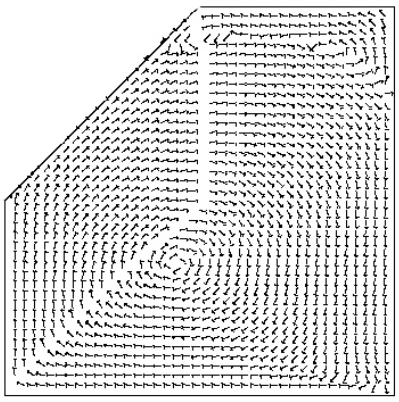

Figure 9. *CFX* results for $Re = 400$

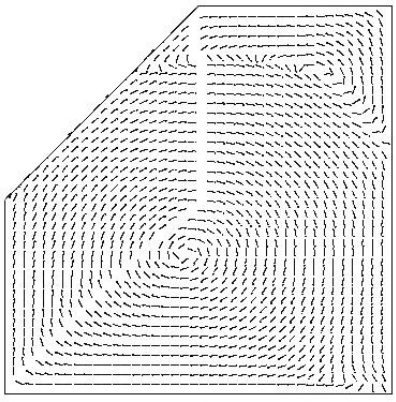

Figure 10. *CFX* results for $Re = 1000$

In Fig. 11, the transverse-integrated u velocity, $\overline{u}^{yt}$, along the vertical line passing through point B of the cavity at a Reynolds number of $Re = 400$ is shown. In this plot, the transverse-integrated velocity, $\overline{u}^{yt}$, is plotted against the y coordinate of the center of the respective node. Furthermore, the results for mesh D, which is a high-resolution mesh that uses a node size that is half the node size of mesh C, are shown in the velocity profile, as well. Since meshes C and D have relatively high degress of resolution, a Richardson extrapolation can be performed using the flow fields calculated on these meshes. In [15], it is shown that the NI-FAM for the convection-diffusion equation is not quite second order, but much better than first order. To determine the order of the NI-FAM numerically, two sets of Richardson extrapolation are performed — the first set assumes that the NI-FAM is first order and the second set assumes that the NI-FAM is second order. In the first set, a second order extrapolation is obtained, while a third order extrapolation is obtained in the second set. These extrapolations are also shown in Fig. 11.

In Fig. 11, the velocity profile calculated on mesh A is clearly inaccurate, however, the general structure of the profile qualitatively agrees with the other velocity profiles. In addition, the velocity profiles calculated on meshes C and D match more closely the third order extrapolation than the second order extrapolation. This suggests that the NI-FAM is indeed close to being a second order method in x and y. In Fig. 11, it is also clearly evident that the velocity profiles converge to a single velocity profile as the meshes are refined. As expected, a similar analysis using the velocity profile for the transverse-integrated v velocity along the vertical passing through point B of the cavity yields results consistent with those discussed here.

4. CONCLUSIONS

The hybrid nodal-integral/finite-analytic method has been extended to solve the time-dependent, incompressible Navier-Stokes equations in two-dimensional arbitrary geometries. For the test problem of viscous fluid flow in an enclosed five-sided cavity, the NI-FAM predicts the existence of a secondary vortex near the top of the cavity accompanied by a clear flow separation point along the right boundary for Reynolds numbers of $Re = 400$ and $Re = 1000$. This flow structure inside the five-sided cavity is confirmed by calculations using the commercial software package, *CFX*. The results of this test problem clearly demonstrate that the NI-FAM is an accurate numerical method capable of simulating (laminar) fluid flow in complex geometries using relatively coarse meshes.

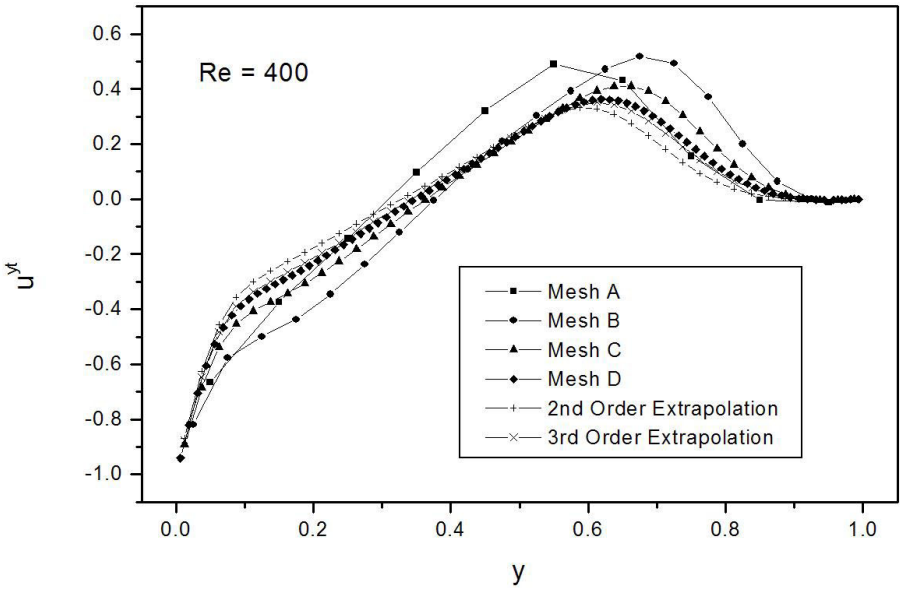

Figure 11. Transverse-integrated u velocity ($\overline{u}^{yt}$) along the vertical line passing through point B of the cavity for $Re = 400$.

ACKNOWLEDGEMENTS

The authors acknowledge the assistance of Daniel Rock with the *CFX* calculations performed for this paper. This research was supported in part by the Department of Nuclear, Plasma, and Radiological Engineering, University of Illinois at Urbana-Champaign and in part by the Center for Simulation of Advanced Rockets, University of Illinois at Urbana-Champaign. The Center is supported by the U.S. Department of Energy through the University of California under subcontract B341494. This work was performed under the auspices of the U.S. Department of Energy by the University of California, Lawrence Livermore National Laboratory under contract No. W-7405-Eng-48.

REFERENCES

[1] AEA Technology plc., *CFX-4.2 Solver*, Oxfordshire, UK (1997).

[2] Y.Y. Azmy, "A Nodal Integral Method for the Numerical Solution of Incompressible Flow Problems," M.S. Thesis, University of Illinois at Urbana-Champaign (1982).

[3] O.R. Burgraf, "Analytical and Numerical Studies of the Structure of Steady Separated Flows," *Journal of Fluid Mechanics*, **24**, pp. 113-151 (1966).

[4] C.J. Chen, R. Bertatz, K.D. Carlson, W. Lin, *Finite Analytic Methods in Flows and Heat Transfer*, Taylor and Francis, New York, U.S.A. (2000).

[5] J.H. Darr, S.P. Vanka, "Separated Flow in a Driven Trapezoidal Cavity," *Physics of Fluids A*, **3**, pp. 385-392 (1991).

[6] H.D. Fisher, H. Finnemann, "The Nodal Integration Method — A Diverse Solver for Neutron Diffusion Problems," *Atomkernenergie*, **39**, pp. 229-236 (1981).

[7] U. Ghia, K.N. Ghia, T. Shin, "High-Re Solutions for Incompressible Flow Using the Navier-Stokes Equatons and a Multigrid Method," *Journal of Computational Physics*, **48**, pp. 387-411 (1982)

[8] S.T. Kim, J.J. Dorning, "Discrete Nodal and Sn Transport Methods for Boundary-Fitted Coordinate Geometries," *Proceedings of the Topical Meeting on Advanced Nuclear Engineering Computation and Radiation Shielding,* **1**, pp. 2:1-2:15 (1989).

[9] E.P.E. Michael, "A Nodal Integral Method for the Linear Steady State Convecton-Diffusion Equation," M.S. Thesis, University of Virginia (1995).

[10] F. Pan, A. Acrivos, "Steady Flows in Rectangular Cavities," *Journal of Fluid Mechanics*, **28**, pp. 643-655 (1967).

[11] D.F. Roscoe, "New Methods for the Derivation of Stable Difference Representations for Difference Equations," *J. Inst. Mathematical Apps.*, **16**, pp. 291-301 (1975).

[12] J.C. Tannehill, D.A. Anderson, R.H. Pletcher, *Computational Fluid Mechanics and Heat Transfer*, Taylor and Francis, Philadelphia, U.S.A. (1997).

[13] A.J. Toreja, Rizwan-uddin, "Hybrid Numerical Methods for the Convection-Diffusion Equation in Arbitrary Geometries," *Proceedings of the International Conference on Mathematics and Computation, Reactor Physics and Environmental Analysis in Nuclear Applications* , Madrid Spain, September 1999, pp. 1705-1714 (1999).

[14] A.J. Toreja, Rizwan-uddin, "A Hybrid Numerical Method for Time-Dependent Convection-Diffusion Problems in Arbitrary Geometries," *Transactions of the American Nuclear Society*, **83**, pp. 426-428 (2000).

[15] A.J. Toreja, "A Nodal Approach to Arbitrary Geometries and Adaptive Mesh Refinement for the Nodal Method," Ph.D. Thesis, University of Illinois at Urbana-Champaign (2002).

[16] A.J. Toreja, Rizwan-uddin, "Hybrid Numerical Methods For Convection-Diffusion Problems in Arbitrary Geometries," accepted for publication in *Computers and Fluids* (2002).

[17] F. Wang, Rizwan-uddin, "A Modified Nodal Scheme for the Time-Dependent Incompressible Navier-Stokes Equations," *submitted for publication* (2002).

[18] B.L. Wescott, Rizwan-uddin, "An Efficient Formulation of the Modified Nodal Integral Method and Application to 2-D Burger's Equation," *Nuclear Science and Engineering*, **139**, pp. 293-505 (2001)

[19] B.L. Wescott, "Efficient Formulation of the Modified Nodal Integral Method and Development of Implicit, Explicit, and Multigrid Schemes Applied to the Two-Dimensional Burger's Equation," M.S. Thesis, University of Illinois at Urbana-Champaign (2001).

[20] G.L. Wilson, "Time-Dependent Nodal Integral Methods in Heat Transfer and Fluid Dynamics," Ph.D. Thesis, University of Virginia (1987).